GPS Solutions (2019) 23:107
https://doi.org/10.1007/s10291-019-0884-5

ORIGINAL ARTICLE

GEO-pivoted carrier ambiguity resolution: a method for instantaneous ambiguity resolution in mid-low-latitude regions

Feng-Yu Chu[1] · Ming Yang[1] · Yan-Ting Chen[1]

Received: 9 August 2018 / Accepted: 27 June 2019 / Published online: 6 August 2019
© Springer-Verlag GmbH Germany, part of Springer Nature 2019

Abstract
The effect of DD ionospheric delays can be unexpectedly large in the range of the equatorial anomaly, that is, in mid-low-latitude regions near noon and/or afternoon, and the large delays cause instantaneous AR to fail even over short baselines. Ionospheric delays can be represented by a function of vertical total electron content values, which often have significant latitudinal gradients in mid-low-latitude regions near noon and/or afternoon. Therefore, a short separation between the pivot and secondary satellites in the latitudinal direction indicates smaller effects of DD ionosphere. In the BeiDou system (BDS), five geostationary earth orbit (GEO) satellites are nearly motionless over the equator. We can use adjacent GEO satellites to form a DD pair whose pivot and secondary satellites are close in latitude ($<4°$). Moreover, when inclined geosynchronous orbit or medium earth orbit (IGSO/MEO) satellites approach the equator, the separations between the IGSO/MEO and GEO satellites in the latitudinal direction will be minimal. Therefore, this study proposes a method called GEO-pivoted carrier AR (GEOCAR) for instantaneous AR. This method mitigates the influence of DD ionospheric delays by pivoting GEO satellites in BDS DD pairs and uses a trade-off design between the ionosphere-fixed and ionosphere-weighting models to resolve integer ambiguities of dual-frequency phases. Experimental short-baseline data (<10 km) collected in mid-low-latitude regions near noon and afternoon are tested with conventional AR and GEOCAR methods. The results show that the GEOCAR can effectively produce higher success percentages than the conventional AR with improvements reaching 68.62% for BDS and 42.55% for BDS/GPS.

Keywords BeiDou system · Instantaneous ambiguity resolution · Mid-low-latitude regions · Single-epoch real-time kinematic positioning

Introduction

Global navigation satellite system (GNSS) real-time kinematic (RTK) positioning determines the relative position between reference and rover receivers using double-differenced (DD) phase and code measurements. Unknown integer phase ambiguities must be resolved to achieve precise and accurate positioning results. The process of resolving integer ambiguities is called ambiguity resolution (AR) (Teunissen 1998) that consists of three generalized steps, (1) obtaining the least-squares estimates of real-value ambiguities, (2) using an integer mapping function to fix the corresponding integer ambiguities, and (3) using the integer ambiguities as constraints in the least-squares adjustment to obtain centimeter-level fixed solutions (Verhagen 2004).

The effect of ionospheric delays on GNSS phase and code measurements can critically affect AR performance. Ionospheric delays are a function of the vertical total electron content (VTEC) and the frequencies of the measurements. VTEC values change with time and the ionospheric pierce point (IPP) of a satellite (Misra and Enge 2006). When the IPPs are stationary, the ionospheric delays can fully reflect the temporal variations such as the diurnal and seasonal variations (Wu et al. 2014; Kunitsyn et al. 2016). Diurnal variation indicates that the ionospheric delays increase near noon, and the maximum magnitude appears near 14:00 local time (Muhtarov and Kutiev 1999; Cander and Mihajlovic 2005), whereas seasonal variation shows that ionospheric delays become relatively large in spring and autumn (Rishbeth and Mendillo 2001). Conversely, if the IPPs change with time, then the ionospheric delays reflect not only the temporal

✉ Ming Yang
myang@mail.ncku.edu.tew

[1] Department of Geomatics, National Cheng Kung University, Tainan, Taiwan

but also the spatial variations. In addition, in the range of the geomagnetic equatorial anomaly (Aderson 1973), i.e., mid-low-latitude region, the VTEC values can be unexpectedly large near noon and/or afternoon. During these periods, VTEC values have significant latitudinal gradients (Klobuchar 1987; Yoshihara and Saito 2004), which are likely to dominate the longitudinal gradients (Strangeways 2000; Abdukkah et al. 2007).

Single-epoch GNSS RTK positioning is immune to cycle slips and re-initializes after loss-of-lock (Parkins 2010). Successful instantaneous AR, the key to single-epoch RTK positioning, can be achieved if the effect of DD ionospheric delays is small and negligible (Li et al. 2014). DD ionospheric delays are generally assumed negligible over short baselines such as 10 km. However, in mid-low-latitude regions, the DD ionospheric delays are often too large to be neglected near noon and/or afternoon, even for short baselines. Consequently, studies indicate that instantaneous AR cannot work satisfactorily in mid-low-latitude regions (Wielgosz et al. 2005; Lejeune and Warnant 2008).

As previously mentioned, VTEC values in mid-low-latitude regions have significant latitudinal gradients, which often dominate the longitudinal gradients. Therefore, if the separation of the pivot and secondary satellites in the latitudinal direction is shortened, then the effect of DD ionospheric delays for a DD pair decreases. However, using two medium earth orbit (MEO) satellites to form a DD pair and keep the pivot and secondary satellites constantly close to each other in the latitudinal direction is difficult because MEO satellites move constantly around the earth. In the current GNSS, the BeiDou system (BDS) is fully operational in the Asia-Pacific region (Chen et al. 2009). Unlike GPS, which is only composed of MEO satellites, the BDS comprises three types of navigation satellites, namely, geostationary earth orbit (GEO), inclined geosynchronous orbit (IGSO), and MEO satellites (CSNO 2013). MEO and IGSO satellites move constantly, whereas GEO satellites are nearly motionless over the equator, i.e., the maximum movement in the latitudinal direction reaches approximately 2° (Montenbruck et al. 2013). Therefore, we can use adjacent GEO satellites to form DD pairs whose pivot and secondary satellites are consistently close in the latitudinal direction (<4°). Moreover, when an IGSO or MEO (I/M) satellite approaches the equator, the separations between the I/M and GEO satellites in the latitudinal direction will become small.

Pivoting DD pairs on GEO satellites is a potential means to form sufficiently small DD ionospheric delays over short baselines in mid-low-latitude regions. As a result, we propose a method for instantaneous AR over short baselines. The proposed method pivots BDS DD measurements on the GEO satellites and manipulates different GNSS models to resolve integer ambiguities. To examine the performance of the proposed method, we collected experimental short-baseline data

Table 1 Orbital types of BDS satellites (CSNO 2013)

Type	Altitude (km)	Ground track repeat period (sidereal day)
GEO	35,786	1
IGSO	35,786	1
MEO	21,528	7

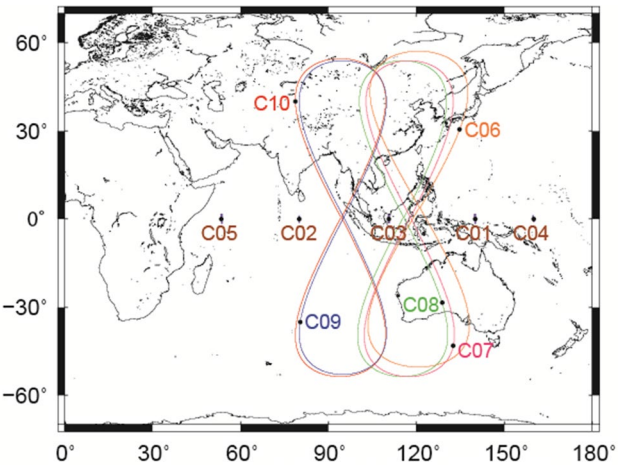

Fig. 1 Ground tracks of BDS GEO and IGSO satellites

(< 10 km) with high VTEC values (70–100 TECU) in a mid-low-latitude region near noon and afternoon, and we tested the data with the proposed method and a conventional AR method.

GPS and BDS DD measurements

GPS and BDS MEO satellites are distributed worldwide, whereas BDS IGSO and GEO satellites are distributed over the Asia-Pacific region. The ground tracks of the GEO satellites are nearly motionless points, and those of the IGSO satellites are represented as figure-of-eight loops. Table 1 shows relevant information of BDS satellites, and Fig. 1 presents the ground tracks of the GEO and IGSO satellites.

The DD measurements suffer from reduced ionospheric and tropospheric delays, and are expressed as follows (Leick et al. 2015):

$$\Delta\nabla\Phi_i = \Delta\nabla\rho + \Delta\nabla T + \lambda_i \cdot \Delta\nabla N_i - \frac{f_1^2}{f_i^2} \cdot \Delta\nabla I + \varepsilon_{\Delta\nabla\Phi_i} \tag{1}$$

$$\Delta\nabla P_i = \Delta\nabla\rho + \Delta\nabla T + \frac{f_1^2}{f_i^2} \cdot \Delta\nabla I + \varepsilon_{\Delta\nabla P_i} \tag{2}$$

Table 2 Carrier signals of GPS and BDS

	Subscript	Signal	Frequency (MHz)	Wavelength (cm)
GPS	1	L1	1575.42	19.03
	2	L2	1227.60	24.42
BDS	1	B1	1561.098	19.20
	2	B2	1207.140	24.83

where $\Delta\nabla$ represents the DD operator, f is the frequency, ρ is the geometric distance between the satellite and the receiver, I is the ionospheric delay based on the frequency f_1, T is the tropospheric delay, N is the integer ambiguity, λ is the wavelength, and ε is the noise plus multi-path effect. For the BDS measurements, the term ε also includes the so-called BDS satellite-induced code bias (Zhang et al. 2017; Chen et al. 2018). The symbols Φ and P are the phase and code measurements, respectively. The subscript i in (1) and (2) refers to the frequency, as listed in Table 2. In this study, the DD phase and code measurement are assumed to be mutually independent.

Behavior of ionospheric delays pivoting on GEO satellites

In this section, we demonstrate the behavior of DD ionospheric delays pivoting on GEO satellites. We collected a 45-km baseline in a mid-low-latitude region (Taiwan, latitude ≅ 22.69°, longitude ≅ 120.36°) in spring for 11 consecutive days.

Figure 2 shows the averages and standard deviations of the 11-day VTEC values. The ground track repeat period of the GEO and IGSO satellites is one day (Table 1). Therefore, we can calculate the averages and standard deviations of the 11-day DD ionospheric delays to represent the expected 1-day variations, as shown in Figs. 3 and 4. The GEO satellite C05 is excluded from this study because this satellite is far from the test area and its signal strength received is low.

A comparison of Figs. 3 and 4 shows that the averages and standard deviations of the IGSO–GEO DD ionospheric delays change more dramatically than those of the GEO–GEO (G–G) DD ionospheric delays when the ionospheric condition is not quiet (10:00–20:00 local time) because the IPPs of IGSO satellites change with time. If the IPPs of IGSO satellites change with time, then the IGSO–GEO DD ionospheric delays reflect not only temporal but also spatial variations. On the other hand, Fig. 4 shows that the averages and standard deviations of the IGSO–GEO DD ionospheric delays decrease when the IGSO satellites move near the equator, e.g., at approximately 13:00, 20:00, and 16:00 local time in the top-left, top-right, and middle-left graphs, respectively. This is because the VTEC values

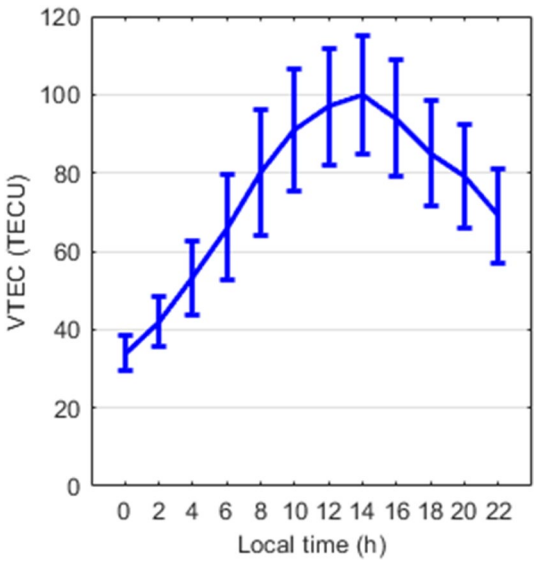

Fig. 2 Mean values and standard deviations of VTEC values over Taiwan for 11 consecutive days (April 2–12, 2015). The VTEC values for each day are obtained by IONEX from the International GNSS Service, and the mean value can peak at 100 TECU at 14:00 local time

on the IPPs can be similar when the IPPs of the pivot and secondary satellites become close. In other words, the averages and standard deviations of the IGSO–GEO DD ionospheric delays vary significantly when the IGSO satellites are far from the equator, e.g., at approximately 14:00 local time in the top-right graph.

Expected one-day variations of MEO–GEO DD ionospheric delays cannot be obtained because of the seven-day ground track repeat period of BDS MEO satellites (Table 1). Thus, we calculate MEO–GEO DD ionospheric delays for seven consecutive days in Fig. 5 to understand the behavior. The figure shows that when one MEO satellite approaches the equator, the DD ionospheric delays decrease, which implies that the behavior of MEO–GEO DD ionospheric delays is similar to that of IGSO–GEO DD ionospheric delays. The bottom-right panel illustrating the RMS value versus latitude shows that statistically, the influence of DD ionospheric delay is minimized at the equator and begins to increase when the secondary satellite moves away from the equator.

Methods

In this section, two methods for instantaneous AR are introduced. One is the conventional AR method, and the other is the proposed new AR method called GEO-pivoted carrier AR (GEOCAR). The two methods are described for the case of combining BDS and GPS measurements. Loosely coupled

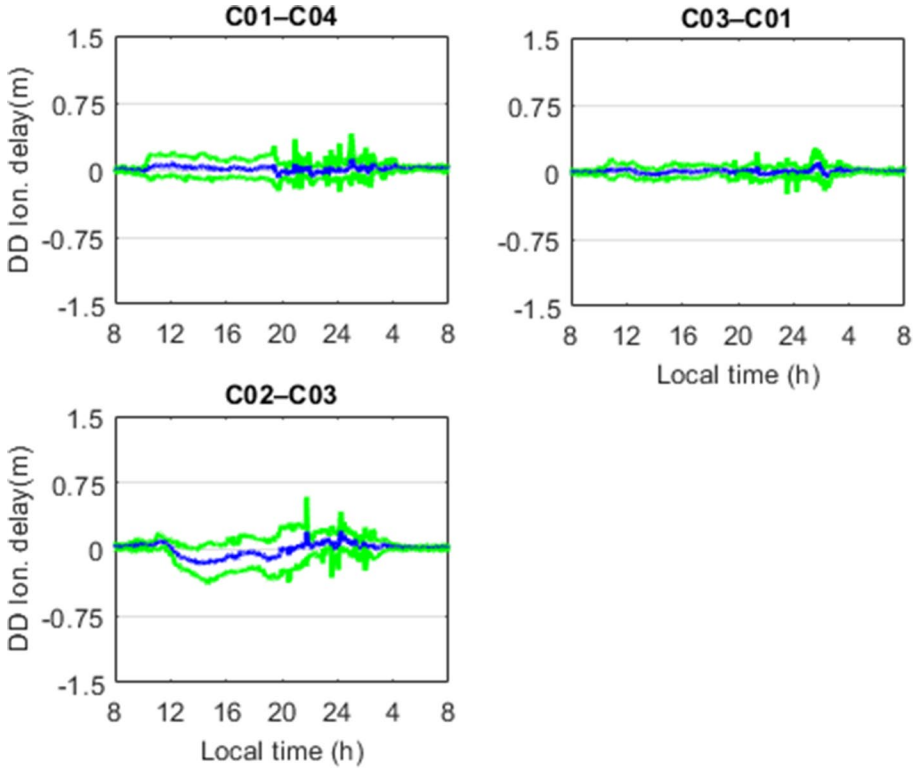

Fig. 3 Mean values and standard deviations for expected one-day DD ionospheric delays composed of adjacent GEO satellites (GEO–GEO); the cutoff angle is 15°. The mean values are indicated by the blue lines, and the standard deviations (1 sigma) by the green lines

pairs are adopted for the combined BDS/GPS data; that is, each constellation uses its own pivot satellite for its respective DD measurements. More detailed information of the loosely coupled pairs can be found in Chu and Yang (2014) and Yang et al. (2018).

Conventional AR method

The conventional AR method has been widely used for current applications of RTK positioning. In this study, it is assumed that the tropospheric delays in (1) and (2) are negligible and the linearized observation equation is expressed as:

$$\begin{cases} E(\mathbf{y}) = \mathbf{Aa} + \mathbf{Bb} + \mathbf{Cc}, \quad D(\mathbf{y}) = \mathbf{Q_{yy}} \\ \breve{\mathbf{a}}_{\mathrm{WL}} = \mathbf{Ha} \end{cases} \tag{3}$$

where $\breve{\mathbf{a}}_{\mathrm{WL}}$ is a pre-determined solution of integer wide-lane (WL) ambiguities. The related derivation of the solution can be found in Tang et al. (2014) and Chu et al. (2014). The solution of integer WL ambiguities has been widely used for improving AR performance. Detailed information of the WL ambiguities of GPS and BDS can be found in Chu et al. (2016) and Chu and Yang (2018), respectively. The parameter vector of the baseline components is as follows:

$$\mathbf{b} = [\, \mathrm{d}x \;\; \mathrm{d}y \;\; \mathrm{d}z \,]^{\mathrm{T}} \tag{4}$$

The parameter vector of the ionospheric delays is as follows:

$$\mathbf{c} = \left[\, \Delta\nabla\mathbf{I}^{\mathrm{B}}_{1\times m} \;\; \Delta\nabla\mathbf{I}^{\mathrm{G}}_{1\times n} \,\right]^{\mathrm{T}} \tag{5}$$

and the vector of the integer phase ambiguities is

$$\mathbf{a} = \left[\, \Delta\nabla\mathbf{N}_{\mathrm{B1},1\times m} \;\; \Delta\nabla\mathbf{N}_{\mathrm{B2},1\times m} \;\; \cdots \;\; \cdots \;\; \Delta\nabla\mathbf{N}_{\mathrm{L1},1\times n} \;\; \Delta\nabla\mathbf{N}_{\mathrm{L2},1\times n} \,\right]^{\mathrm{T}} \tag{6}$$

The vector $\mathbf{y}$ represents the observation minus computed range and is assumed to be contaminated by normally distributed noise with zero mean and variance matrix $\mathbf{Q_{yy}}$. Matrices $\mathbf{A}$, $\mathbf{B}$, and $\mathbf{C}$ are the design matrices corresponding to vectors $\mathbf{a}$, $\mathbf{b}$, and $\mathbf{c}$, respectively. Matrix $\mathbf{H}$ is the design matrix for $\breve{\mathbf{a}}_{\mathrm{WL}}$.

Additional information of a priori DD ionospheric delay, denoted as $\mathbf{c}_0$, is usually incorporated with (3) to facilitate AR performance. The a priori DD ionospheric delay is generally given as (Yang et al. 2000),

$$E(\mathbf{c}_0) = 0, \quad D(\mathbf{c}_0) = \mathbf{Q}_{\mathbf{c}_0\mathbf{c}_0} \tag{7}$$

and the variance matrix is

$$\mathbf{Q}_{\mathbf{c}_0\mathbf{c}_0} = \sigma^2_{\Delta\nabla I} \cdot \mathbf{e}_{(m+n)\times(m+n)} \tag{8}$$

where $\boldsymbol{e}$ is an identity matrix. If the sigma $\sigma_{\Delta\nabla I}$ of the a priori DD ionospheric delay is given as zero, the parameter vector of the DD ionospheric delays in (5) will not be estimated; in this case, the process of the conventional method is referred to as the ionosphere-fixed model. By contrast, if the sigma

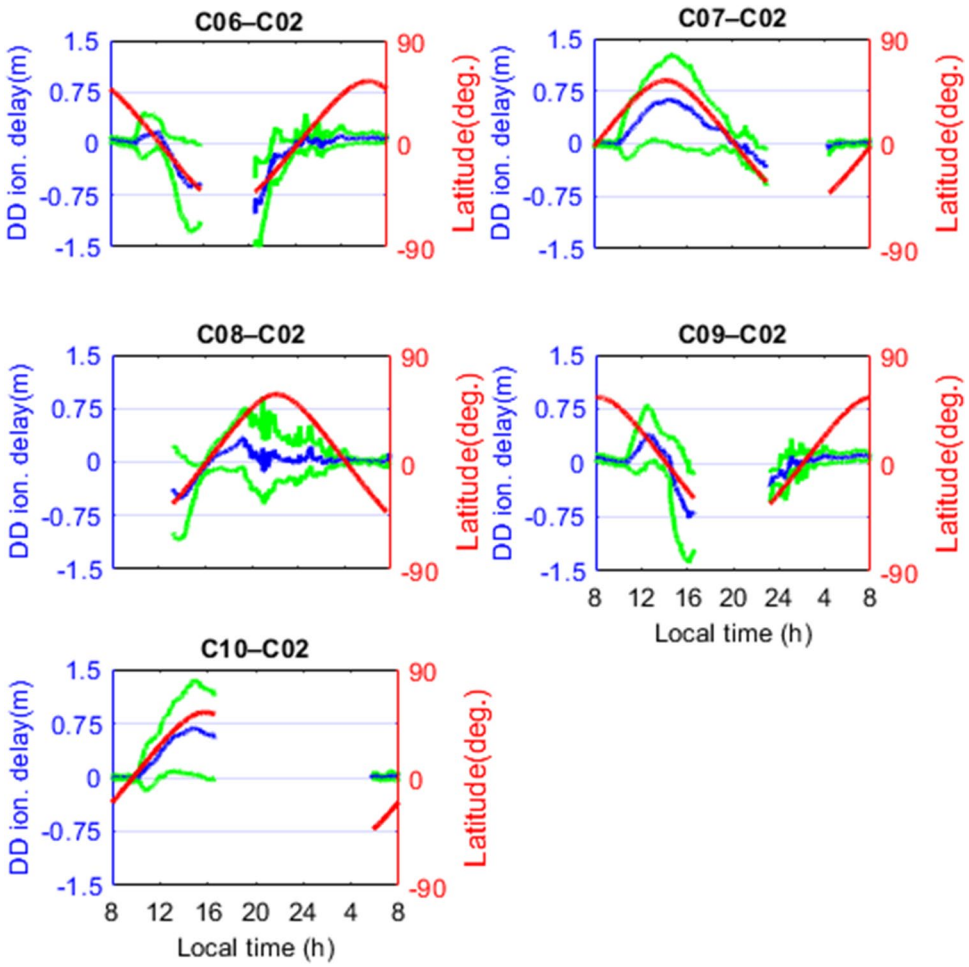

Fig. 4 Mean values and standard deviations for expected one-day DD ionospheric delays composed of one secondary IGSO satellite and pivot GEO satellite (IGSO–GEO); the cutoff angle is 15°. The blue lines are the mean values, and the green lines are the standard deviations (1 sigma). The geographical latitudes of the secondary satellites are shown by the red lines

$\sigma_{\Delta\nabla I}$ is given as a nonzero value, the ionospheric parameter vector will be estimated, and in this case, the process of the conventional method is called the ionosphere-weighting model (Odijk et al. 2000).

Since the ionosphere-weighting model estimates the ionospheric parameters, whereas the ionosphere-fixed model does not, the measurement redundancy number of the ionosphere-fixed model is higher than that of the ionosphere-weighting model. Consequently, the ionosphere-fixed model has stronger model strength and produces better AR performance than the ionosphere-weighting model when the DD ionospheric delay is sufficiently small (i.e., < 10 cm). On the other hand, when the DD ionospheric delay is not small (i.e., ≥ 10 cm), the ionosphere-weighting model prevails over the ionosphere-fixed model in AR performance. More information about the individual strength of the two models can be found in Li et al. (2014).

After the vector of real-value phase ambiguities, denoted as $\hat{\mathbf{a}}$, is computed, the LAMBDA method (Teunissen 1995) is used to recover the vector of integer values $\breve{\mathbf{a}}$. Moreover, the ratio test (Verhagen and Teunissen 2013) is used to validate the resolved integer phase ambiguities.

GEOCAR method

As mentioned previously, the ionosphere-fixed model produces better AR performance when the effect of DD ionospheric delays is sufficiently small. Conversely, the ionosphere-weighting model prevails in the presence of large DD ionospheric delays. Since the size of DD ionospheric delays constantly changes and can be unexpected large in mid-low latitudes even over short baselines, the GEOCAR method develops a trade-off design between the ionosphere-fixed and -weighting models to take advantage of both models. Moreover, the method adopts DD pairs pivoted on GEO satellites to achieve AR. At present, the method is mainly designed for BDS in the Asia-Pacific because BDS has deployed its own GEO satellites in this region. The method can be applied to multiple-constellation cases on the basis of BDS, e.g., BDS/GPS, BDS/Galileo, BDS/GPS/Galileo. Each constellation uses its own pivot satellite for its respective DD measurements. For the case of BDS/GPS used in this study, BDS DD pairs are pivoted on GEO satellites, and GPS DD pairs are pivoted on the MEO satellite with the highest elevation angle.

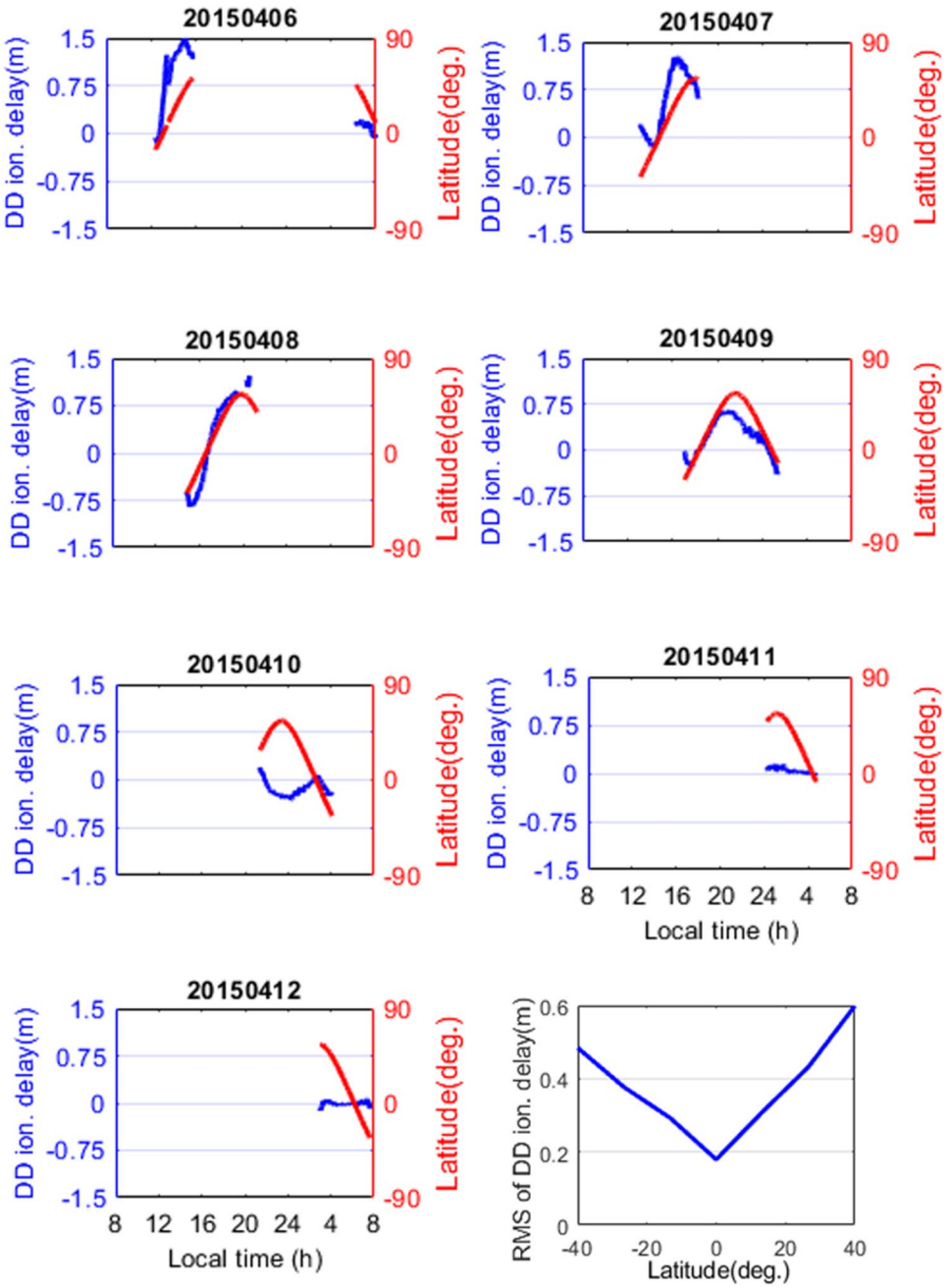

Fig. 5 DD ionospheric delays composed of MEO satellite C11 and pivot GEO satellite C02 (MEO–GEO) for consecutive days during April 6–12, 2015. The cutoff angle is 15°. Blue lines indicate the DD ionospheric delays, and the geographical latitudes of the MEO satellites are shown by the red lines. Bottom-right panel shows the RMS of DD ionospheric delays versus latitude

The trade-off design first uses the ionosphere-fixed model to resolve a subset of real-value ambiguities that are affected by sufficiently small DD ionosphere delays, denoted as $\hat{\mathbf{a}}_{\text{sub}}$. The corresponding integer solution $\breve{\mathbf{a}}_{\text{sub}}$ can be recovered immediately by the LAMBDA method as a result of the good model strength of the ionosphere-fixed model. The subset $\breve{\mathbf{a}}_{\text{sub}}$ is then treated as an additional constraint for the ionosphere-weighting model to improve its performance because the strength of the ionosphere-weighting model is weaker than that of the ionosphere-fixed model. The linearized observation equation of the ionosphere-weighting model is expressed as follows:

$$\begin{cases} E(\mathbf{y}_2) = \mathbf{Aa} + \mathbf{Bb} + \mathbf{Cc}, \quad D(\mathbf{y}_2) = \mathbf{Q}_{\mathbf{y}_2\mathbf{y}_2} \\ E(\mathbf{c}_0) = \mathbf{Cc}, \quad D(\mathbf{c}_0) = \mathbf{Q}_{\mathbf{c}_0\mathbf{c}_0} \\ \breve{\mathbf{a}}_{\text{WL}} = \mathbf{Ha} \\ \breve{\mathbf{a}}_{\text{sub}} = \mathbf{Ma} \end{cases} \tag{9}$$

where $\mathbf{M}$ is the design matrix of constraint $\breve{\mathbf{a}}_{\text{sub}}$. Once the strength of the ionosphere-weighting model is improved by the constraint, the integer ambiguities $\breve{\mathbf{a}}$ can be quickly recovered by the LAMBDA method.

The GEOCAR method forms two types of DD pairs for BDS, namely G–G and I/M–GEO (I/M–G) pairs. To make the influence of DD ionospheric delays in each pair as small as possible, the method selects the pivot GEO satellite that is closest to the secondary satellite. Subsets of $\mathbf{a}$, denoted as $\mathbf{a}_{sub}^{ith}$, are formed. The first subset $\mathbf{a}_{sub}^{1st}$ only comprises G–G pairs formed with adjacent GEO satellites. These pairs are C01–C04, C01–C03, and C03–C02, of which separations are small ($<4°$) in the latitudinal direction and not too large ($<31°$) in the longitudinal direction. Compared with $\mathbf{a}_{sub}^{1st}$, the second subset $\mathbf{a}_{sub}^{2nd}$ comprises one more I/M–G pair, where the I/M satellite has the lowest latitude (denoted as I/M^{1st}) and the GEO satellite is closest to the I/M satellite in the longitudinal direction. Similarly, one more I/M–G pair is added to $\mathbf{a}_{sub}^{2nd}$, where the I/M satellite has the second lowest latitude (denoted as I/M^{2nd}), to form the third subset $\mathbf{a}_{sub}^{3rd}$. Likewise, the fourth subset $\mathbf{a}_{sub}^{4th}$ is formed with an additional I/M^{3rd}–G pair, and so on.

Figure 6 presents the detailed procedure of the GEOCAR method. In the first loop, the method resolves $\breve{\mathbf{a}}_{sub}^{1st}$ with the ionosphere-fixed model and then replaces $\breve{\mathbf{a}}_{sub}$ with $\breve{\mathbf{a}}_{sub}^{1st}$ in the ionosphere-weighting model in (9). After the real-value ambiguities $\breve{\mathbf{a}}$ are resolved, the integer ambiguities $\breve{\mathbf{a}}$ are recovered by the LAMBDA method and validated by the ratio test. If the ratio test value, denoted as Ratio^{1st}, is smaller than the given threshold of the ratio test, the method proceeds to the second loop. In the second loop, the method

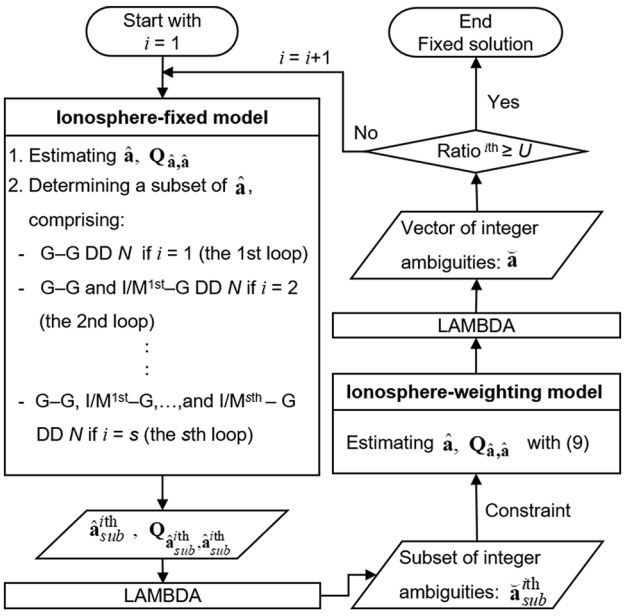

Fig. 6 Procedure of the GEOCAR method (s I/M satellites are assumed). The method is implemented with several loops (up to s loop). In each loop, the ionosphere-fixed model produces its respective subset of $\breve{\mathbf{a}}$, to be used as an additional constraint by the ionosphere-weighting model

similarly resolves $\breve{\mathbf{a}}_{sub}^{2nd}$ with the ionosphere-fixed model and replaces $\breve{\mathbf{a}}_{sub}$ with $\breve{\mathbf{a}}_{sub}^{2nd}$ in (9). Since $\breve{\mathbf{a}}_{sub}^{2nd}$ has one more DD ambiguity than $\breve{\mathbf{a}}_{sub}^{1st}$, the strength of the ionosphere-weighting model in the second loop should be better than that in the first loop, and the ratio test value in the second loop, denoted as Ratio^{2nd}, should be higher than Ratio^{1st}, on the premise that $\breve{\mathbf{a}}_{sub}^{2nd}$ is correct. If Ratio^{2nd} is still smaller than the given threshold, the method proceeds to the third loop. The procedure continues until the ratio test value is larger than or equal to the threshold or no more I/M-G DD ambiguity can be resolved.

Experiment and analysis

In the analysis, the performance of instantaneous AR is evaluated. We adopt four short experimental baseline data, which are collected in Southern Taiwan (a mid-low-latitude region) near noon and afternoon, in an open-sky environment. The test data are also collected in 2014 and 2015, during the ascending half of the solar cycle 24 (Kakoti et al. 2017). Table 3 lists the details of the baseline data.

The reference values of the station coordinates, integer ambiguities, DD ionospheric delays, and relative zenith tropospheric delays over these baseline data are calculated with the static processing of the entire 1-h observation periods because the baseline data are collected in static mode. Table 4 summarizes the strategies of handling measurement errors over these baseline data.

Figures 7, 8, 9, and 10 illustrate the DD ionospheric delays and the root mean square (RMS) over these baselines. Baseline 1 (13 m) is a case in which the influence of DD ionospheric delays is negligible. Figure 7 shows that all DD ionospheric delays are significantly smaller than 5 cm during the observation period. Baselines 2, 3, and 4 are cases in which the influences of DD ionospheric delays are not negligible. Figures 8, 9, and 10 show that the DD ionospheric delays larger than 10 cm are present during

Table 3 Information of test baselines

Baseline name	Length	Observation period (local time)	VTEC values over test baseline	Sampling rate (Hz)
Baseline 1	13 m	15:00–16:00, Oct. 20, 2015	≈ 70	1
Baseline 2	4.0 km	13:00–14:00, Mar. 25, 2014	≈ 100	1
Baseline 3	9.4 km	14:00–15:00, Apr. 9, 2015	≈ 95	1
Baseline 4	9.4 km	14:40–15:40, Apr. 6, 2015	≈ 95	1

Table 4 Processing strategies for handling measurement errors

Measurement errors	Processing strategy
Orbital errors	Reduced with DD technique (broadcast ephemeris)
Satellite and receiver clock errors	Eliminated with DD technique
GNSS time offset	Eliminated with DD technique
Ionospheric delays	Additional ionospheric parameters with a priori DD ionospheric delays
Tropospheric delays	Corrected by using modified Hopfield model (Goad and Goodman 1974) and residual delays assumed negligible with DD technique
Inter-satellite-type bias (Nadarajah et al. 2015)	Homogeneous receivers (Trimble R9)
Elevation cutoff angle	15°
Observation weighting	$\sigma_{\Delta\nabla P} = 60$ cm, $\sigma_{\Delta\nabla\Phi} = 6$ mm (given with typical level) (Hofmann-Wellenhof et al. 2008)

the observation periods. Figure 11 illustrates the relative zenith tropospheric delays over Baselines 1–4. The absolute value of the maximum delay is about 2 cm, which is small enough to be neglected in ambiguity resolution (Li et al. 2014).

We define the success percentage to quantify the performance of instantaneous AR as follows:

$$\text{Success percentage} = \frac{N_{\text{correct}}}{N_{\text{all}}} \times 100\% \tag{10}$$

where N_{all} is the number of total epochs during the observation period and N_{correct} is the number of epochs whose ratio test values are larger than or equal to a threshold of 2 on the premise that the integer ambiguities are correctly fixed. Two cases, namely stand-alone BDS and combined BDS/GPS, are compared to understand the influence of satellite geometry. In addition, we compare the performances of the conventional AR and the GEOCAR methods to understand the improvement of the GEOCAR method.

Figure 12 shows the success percentages over Baseline 1 (13 m). The graph shows the success percentages of the conventional AR method and indicates that the success percentages using $\sigma_{\Delta\nabla I} = 0$ m (i.e., ionosphere-fixed model) reach 100%. However, the success percentages significantly decrease when $\sigma_{\Delta\nabla I}$ becomes large (i.e., ionosphere-weighting model) because the strength of the ionosphere-weighting model is weaker than that of the ionosphere-fixed model. In contrast to the conventional AR method, the success percentages of the GEOCAR method reach 100% for BDS and BDS/GPS when $\sigma_{\Delta\nabla I}$ is 0.2, 0.3, and 0.4 m. This result is caused by all the BDS DD ionospheric delays over Baseline 1 being sufficiently small, and the trade-off design is able to effectively improve the strength of the ionosphere-weighting model.

Figure 13 shows the success percentages over Baseline 2 (4 km). The top graph shows the success percentages of the conventional AR method and indicates that the method fails to resolve the integer ambiguities when $\sigma_{\Delta\nabla I}$ is 0 m because the influence of DD ionospheric delays is non-negligible. In this case, the best success percentages are produced when $\sigma_{\Delta\nabla I}$ is 0.2 m. However, the best success percentages are only 17.39% for BDS and 62.06% for BDS/GPS. The results imply that the conventional AR method does not work reliably for such a short baseline in mid–low-latitude regions. In contrast to the top graph, the bottom graph shows that the GEOCAR method produces success percentages of 98.44% for BDS and 99.00% for BDS/GPS when $\sigma_{\Delta\nabla I}$ is 0.2 m. The improvements in success percentage are 81.05% (98.44–17.39%) for BDS, and 36.94% (99.00–62.06%) for BDS/GPS.

On the other hand, many BDS DD pairs with sufficiently small ionospheric delays exist over this baseline. As shown in the top and center graphs of Fig. 8, the G–G, I/M^{1st}–G, I/M^{2nd}–G, and I/M^{3rd}–G DD ionospheric delays are smaller than 5 cm during the entire observation period. As a result, the trade-off design is able to adequately improve the strength of the ionosphere-weighting model. This condition explains that BDS and BDS/GPS have the similarly high success percentages at each $\sigma_{\Delta\nabla I}$, as shown in the bottom graph of Fig. 13.

Figure 14 shows the success percentages over Baseline 3 (9.4 km). The top graph shows that the conventional AR method produces the best success percentages when $\sigma_{\Delta\nabla I}$ is 0.3 m, that is, 12.19% for BDS and 42.61% for BDS/GPS. In contrast to the top graph, the bottom graph shows that the success percentages of the GEOCAR method reach 96.20% for BDS and 96.39% for BDS/GPS when the same $\sigma_{\Delta\nabla I}$ is used. The improvements of the GEOCAR method in success percentage are 84.01% (96.20–12.19%) for BDS, and 53.78% (96.39–42.61%) for BDS/GPS.

Similar to Baseline 2, Baseline 3 has many BDS DD pairs with sufficiently small ionospheric delays. As shown in the top and medium graphs of Fig. 9, the G–G, I/M^{1st}–G, I/M^{2nd}–G, and I/M^{3rd}–G DD ionospheric delays are smaller than 5 cm during the entire observation period. Therefore, both BDS and BDS/GPS can produce the similarly high

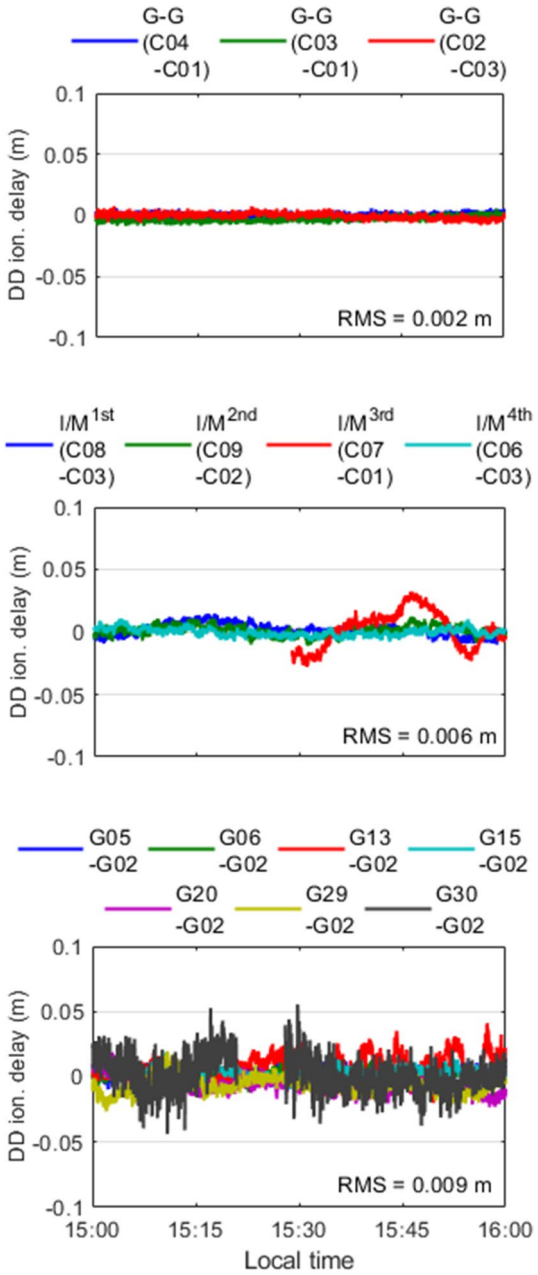

Fig. 7 DD ionospheric delays over Baseline 3 (13 m); (top) BDS G–G DD ionospheric delays, (medium) BDS I/M–G DD ionospheric delays, (bottom) GPS DD ionospheric delays

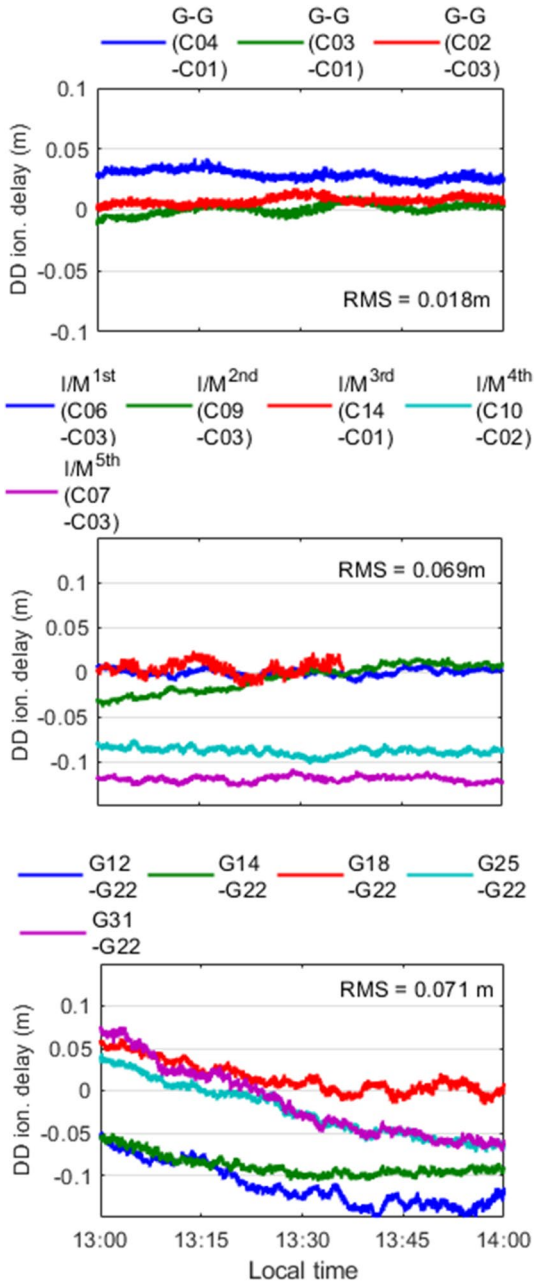

Fig. 8 DD ionospheric delays over Baseline 3 (4 km); (top) BDS G–G DD ionospheric delays, (medium) BDS I/M–G DD ionospheric delays, (bottom) GPS DD ionospheric delays

success percentages at each $\sigma_{\Delta\nabla I}$, as shown in the bottom graph of Fig. 14.

Figure 15 shows the success percentages over Baseline 4 (9.4 km). The success percentages of the conventional AR method are shown in the top graph, where the best success percentages are 9.97% for BDS and 36.75% for BDS/GPS when $\sigma_{\Delta\nabla I}$ is 0.3 m. The bottom graph shows that the GEOCAR method using the same $\sigma_{\Delta\nabla I}$ produces success percentages of 50.78% for BDS and 76.44% for BDS/GPS. The improvements in success percentage are 40.81% (50.78–9.97%) for BDS and 36.96% (75.44–36.75%) for BDS/GPS. Through Figs. 13, 14, and 15, the average improvements are 68.62% ($\frac{81.05\%+84.01\%+40.81\%}{3}$) for BDS and 42.55% ($\frac{36.94\%+53.78\%+36.96\%}{3}$) for BDS/GPS when the influence of DD ionospheric delays is non-negligible.

Meanwhile, Baselines 3 and 4 have the same satellite availability (three BDS G–G, five BDS I/M–G, and seven GPS DD pairs). In addition, Figs. 9 and 10 show that the

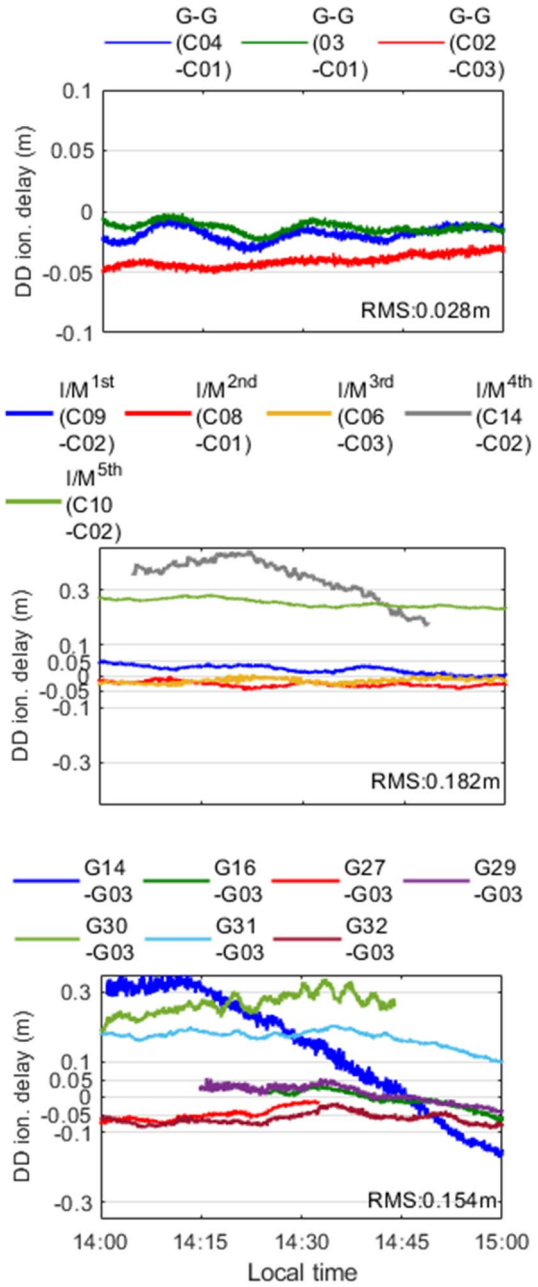

Fig. 9 DD ionospheric delays over Baseline 3 (9.4 km); (top) BDS G–G DD ionospheric delays, (medium) BDS I/M–G DD ionospheric delays, (bottom) GPS DD ionospheric delays

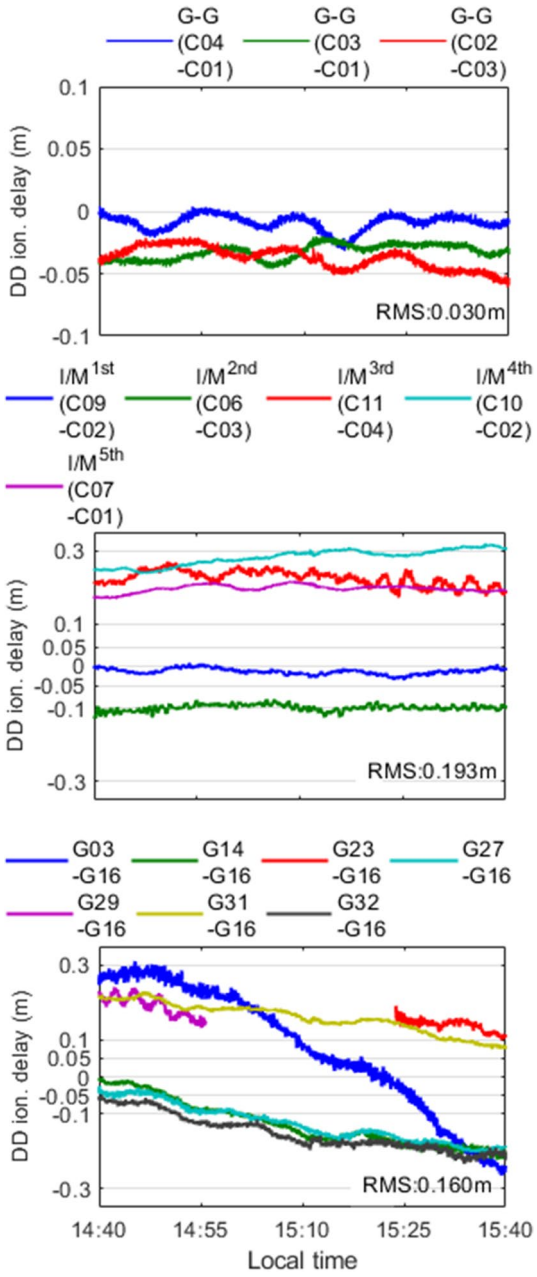

Fig. 10 DD ionospheric delays over Baseline 4 (9.4 km); (top) BDS G–G DD ionospheric delays, (medium) BDS I/M–G DD ionospheric delays, (bottom) GPS DD ionospheric delays

RMS values of BDS G–G, BDS I/M–G, and GPS DD ionospheric delays over Baselines 3 are similar to those over Baseline 4. However, a comparison of the bottom graphs of Figs. 14 and 15 indicates that the success percentages of the GEOCAR method over Baseline 4 are significantly lower than those over Baseline 3. This result is caused by the few BDS DD pairs with sufficiently small ionospheric delays over Baseline 4, which causes the trade-off design to fail to improve the strength of the ionosphere-weighting model for BDS and BDS/GPS adequately. As shown in the top and medium graphs of Fig. 10, only the G–G and I/M^{1st}–G DD ionospheric delays are sufficiently small during the entire observation period.

Table 5 shows the RMS of single-epoch 3D positioning errors. The fixed positioning solutions are adopted for the epochs whose ratio test values are larger than or equal to a given threshold of 2, whereas the float positioning solutions are adopted for the epochs whose ratio test values are smaller than the threshold. The results in Table 5 are computed

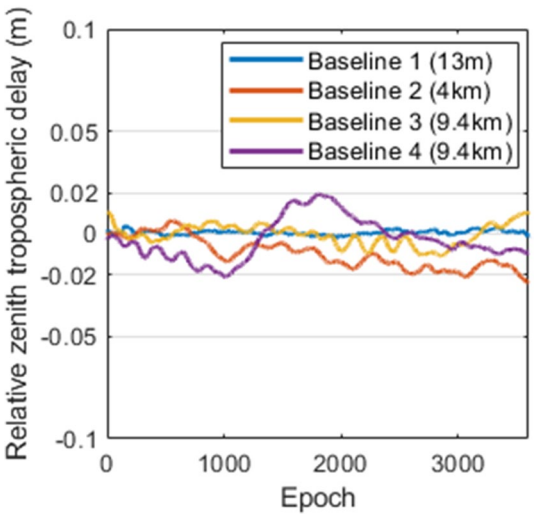

Fig. 11 Relative zenith tropospheric delays over Baselines 1–4

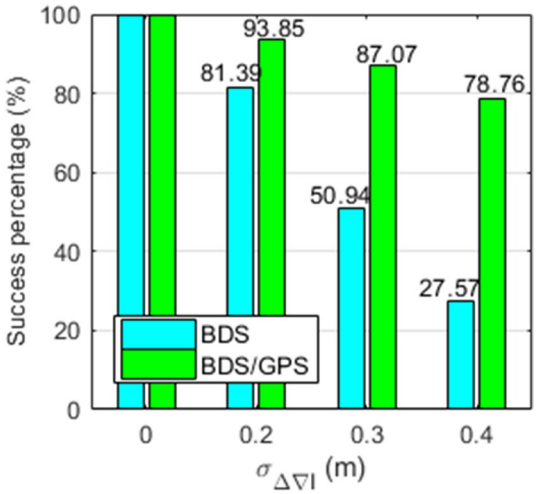

Fig. 12 Success percentages of the conventional AR method over Baseline 1 (13 m)

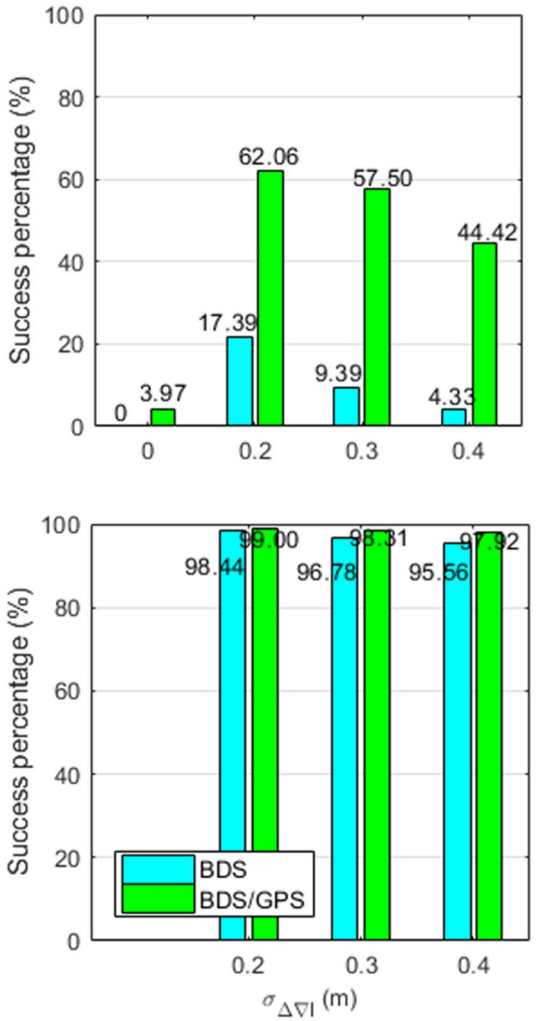

Fig. 13 Success percentages over Baseline 2 (4 km); (top) conventional AR and (bottom) GEOCAR methods

according to the best success percentages, i.e., $\sigma_{\Delta\nabla I}$= 0 m for Baseline 1, $\sigma_{\Delta\nabla I}$= 0.2 m for Baseline 2, $\sigma_{\Delta\nabla I}$= 0.3 m for Baseline 3, and $\sigma_{\Delta\nabla I}$= 0.3 m for Baseline 4. Table 5 shows that the GEOCAR method provides more accurate positioning solutions than the conventional AR method when the influence of DD ionospheric delays is non-negligible (Baselines 2–4), as a result of the higher success percentages produced by the GEOCAR method.

Conclusions

Instantaneous AR can be achieved if the influence of DD ionospheric delays is negligible. In mid–low-latitude regions, the VTEC values have significant latitudinal gradients near noon and/or afternoon, causing the influence of DD ionospheric delays to become non-negligible even over short baselines. Therefore, a shorter separation between the pivot and secondary satellites in the latitudinal direction indicates smaller resulting DD ionospheric delays. This study demonstrates that if a DD pair is pivoted on one GEO satellite that is nearly motionless over the equator, then the ionospheric delay can become small when the secondary satellite is near the equator. We propose a new method called GEOCAR to improve instantaneous AR over short baselines in mid–low-latitude regions. The method pivots BDS DD measurements on GEO satellites and uses a trade-off design between the ionosphere-fixed and -weighting models to resolve integer ambiguities of dual-frequency phases.

The GEOCAR and conventional AR method are used to evaluate the performance of instantaneous AR. Experimental baselines shorter than 10 km are collected in a mid-low-latitude region, near noon and afternoon (VTEC up to 100

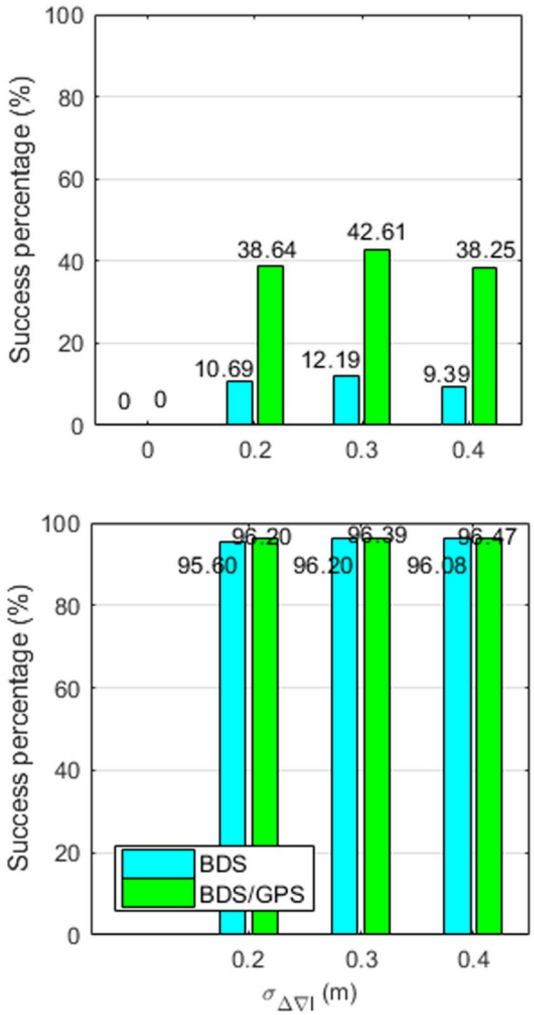

Fig. 14 Success percentages over Baseline 3 (9.4 km); (top) conventional AR and (bottom) GEOCAR methods

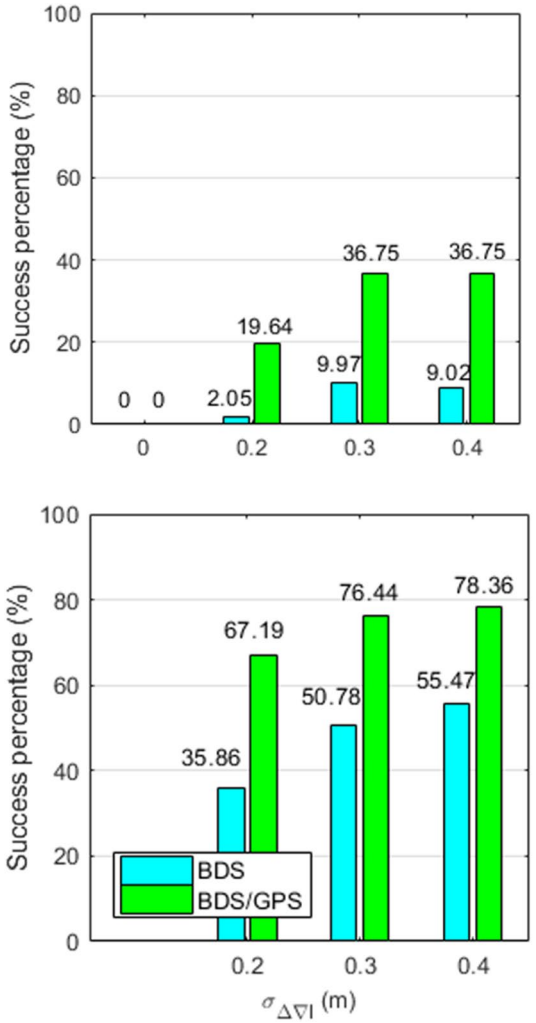

Fig. 15 Success percentages over Baseline 4 (9.4 km); (top) conventional AR and (bottom) GEOCAR methods

TECU). The test results indicate that the GEOCAR and conventional AR methods can similarly produce high success percentages when the influence of DD ionospheric delays is negligible. However, when the influence of DD ionospheric delays is non-negligible, the GEOCAR method generally provides higher success percentages than the conventional AR method; the average improvements obtained from Baselines 2–4 are 68.62% for BDS and 42.55% for BDS/GPS.

This study uses the GEOCAR method to improve the AR performance of single-epoch RTK positioning over a single baseline in an open-sky environment. However, one should note that the multi-path biases associated with BDS GEO satellites, including receiver multi-path and satellite multi-path, could be large enough to affect the AR performance in some constrained environments.

At present, the proposed method is mainly designed for BDS in the Asia-Pacific because BDS has deployed GEO satellites in this region. That is to say; stand-alone GPS cannot utilize the method because GPS does not have GEO satellites. However, in the future, the incoming dual-frequency satellite-based augmentation system (SBAS), e.g., wide area augmentation system (WASS), European geostationary navigation overlay service (EGNOS), Quasi-Zenith satellite system (QZSS), and GPS-aided geo-augmented navigation (GAGAN), will provide worldwide GEO satellites for transmitting GPS-compatible L1 and

Table 5 RMS of single-epoch 3D positioning errors. Unit is meter

Baseline	Conventional AR		GEOCAR	
	BDS	BDS/GPS	BDS	BDS/GPS
1	0.015	0.008	0.015	0.008
2	0.161	0.117	0.045	0.024
3	0.481	0.426	0.138	0.101
4	0.529	0.412	0.354	0.271

L5 frequencies. By then, the method can be updated for worldwide usage.

Acknowledgments This work is supported by the Ministry of Science and Technology (Grant Nos. 107-2219-M-006-025 and 107-2221-E-006-123-MY3) of Taiwan.

References

Abdukkah M, Strangeways HJ, Walsh DMA (2007) Effects of ionospheric horizontal gradients on differential GPS. Acta Geophys 55(4):509–523

Anderson DN (1973) A theoretical study of the ionospheric F region equatorial anomaly—II. Results in the American and Asian sectors. Planet Space Sci 21(3):421–442

Cander LR, Mihajlovic SJ (2005) Ionospheric spatial and temporal variations during the 29–31 October 2003 storm. J Atmos Solar Terr Phys 67(12):1118–1128

Chen H-C, Huang Y-S, Chiang K-W, Yang M, Rau R-J (2009) The performance comparison between GPS and BeiDou-2/COMPASS: a perspective from Asia. J Chin Inst Eng 32(5):679–689

Chen J, Yue D, Zhu S, Chen H, Liu Z, Zhao X (2018) Correction model of BDS satellite-induced code bias and its impact on precise point positioning. Adv Space Res 63(7):2155–2163

Chu F-Y, Yang M (2014) GPS/Galileo long baseline computation: method and performance analyses. GPS Solut 18(2):263–272

Chu F-Y, Yang M (2018) BeiDou system (BDS) triple-frequency ambiguity resolution without code measurements. Remote Sens 10(5):675

Chu F-Y, Yang M, Wu J (2014) Triple-frequency GPS ambiguity resolution for postprocessed medium-range baseline determination: a phase-only method. J Chin Inst Eng 37(3):279–287

Chu F-Y, Yang M, Wu J (2016) A new approach to modernized GPS phase-only ambiguity resolution over long baselines. J Geod 90(3):241–254

CSNO (2013) BeiDou navigation satellite system signal in space interface control document: open service signal, version 2.0. China satellite navigation office, Dec 2013. Available on the internet

Goad CC, Goodman L A (1974) Modified hopfield tropospheric refraction correction model. In: American geophysical union fall meeting. San Francisco, December 12–17, pp 1106–1133

Hofmann-Wellenhof B, Lichtenegger H, Wasle E (2008) GNSS-global navigation satellite systems. Springer, Vienna

Kakoti G, Bhuyan PK, Hazarika R (2017) Seasonal and solar cycle effects on TEC at 95°E in the ascending half (2009–2014) of the subdued solar cycle 24: consistent underestimation by IRI 2012. Adv Space Res 60(2):257–275

Klobuchar JA (1987) Ionospheric time-delay algorithm for single-frequency GPS users. IEEE Trans Aerosp Electron Syst AES-23(3):325–331

Kunitsyn VE, Padokhin AM, Kurbatov GA, Yasyukevich YV, Morozov YV (2016) Ionospheric TEC estimation with the signals of various geostationary navigational satellites. GPS Solut 20(4):877–884

Leick A, Rapoport L, Tatarnikov D (2015) GPS satellite surveying, 4th edn. Wiley, New York

Lejeune S, Warnant R (2008) A novel method for the quantitative assessment of the ionosphere effect on high accuracy GNSS applications, which require ambiguity resolution. J Atmos Solar Terr Phys 70(6):889–900

Li B, Verhagen S, Teunissen PJG (2014) Robustness of GNSS integer ambiguity resolution in the presence of atmospheric biases. GPS Solut 18(2):283–296

Misra P, Enge P (2006) Global positioning system, signal, measurements, and performance, 2nd edn. Ganag-Jamuna Press, Lincoln

Montenbruck O, Hauschild A, Steigenberger P, Hugentobler U, Teunissen P, Nakamura S (2013) Initial assessment of the COMPASS/BeiDou-2 regional navigation satellite system. GPS Solut 17(2):211–222

Muhtarov P, Kutiev I (1999) Autocorrelation method for temporal interpolation and short-term prediction of ionospheric data. Radio Sci 34(2):459–464

Nadarajah N, Teunissen PJG, Sleewaegen J-M, Montenbruck O (2015) The mixed-receiver BeiDou inter-satellite-type bias and its impact on RTK positioning. GPS Solut 19(3):357–368

Odijk D, HvD Marel, Song I (2000) Precise GPS positioning by applying ionospheric corrections from an active control network. GPS Solut 3(3):49–57

Parkins A (2010) Increasing GNSS RTK availability with a new single-epoch batch partial ambiguity resolution algorithm. GPS Solut 15(4):391–402

Rishbeth H, Mendillo M (2001) Patterns of F2-layer variability. J Atmos Solar Terr Phys 63(15):1661–1680

Strangeways HJ (2000) Effect of horizontal gradients on ionospherically reflected or transionospheric paths using a precise homing-in method. J Atmos Solar Terr Phys 62(15):1361–1376

Tang W, Deng C, Shi C, Liu J (2014) Triple-frequency carrier ambiguity resolution for Beidou navigation satellite system. GPS Solut 18(3):335–344

Teunissen PJG (1995) The least-squares ambiguity decorrelation adjustment: a method for fast GPS integer ambiguity estimation. J Geod 70:65–82

Teunissen PJG (1998) Success probability of integer GPS ambiguity rounding and bootstrapping. J Geod 72(1–2):606–612

Verhagen S (2004) Integer ambiguity validation: an open problem? GPS Solut 8(1):36–43

Verhagen S, Teunissen PJG (2013) The ratio test for future GNSS ambiguity resolution. GPS Solut 17(4):535–548

Wielgosz P, Kashani I, Grejner-Brzezinska D (2005) Analysis of long-range network RTK during a severe ionospheric storm. J Geod 79(9):524–531

Wu X, Hu X, Wang G, Zhong H, Tang C (2014) Evaluation of COMPASS ionospheric model in GNSS positioning. Adv Space Res 51(6):959–968

Yang M, Tang C-H, Yu T-T (2000) Development and assessment of a medium-range real-time kinematic GPS algorithm using an ionospheric information filter. Earth, Planets Space 52(10):783–788

Yang M, Chu F-Y, Lin C-Y (2018) GNSS ambiguity resolution in kinematic positioning: benefits of satellite availability and sampling rate. J Aeronaut Astron Aviat 50(2):187–204

Yoshihara T, Saito A (2004) A study of the ionospheric effect on GBAS (Ground-Based Augmentation System) using the nation-wide GPS network data in Japan. In: ION NTM 2004. Institute of Navigation, San Diego, January 26–28, pp 502–511

Zhang X, He X, Liu W (2017) Characteristics of systematic errors in the BDS Hatch–Melbourne–Wübbena combination and its influence on wide-lane ambiguity resolution. GPS Solut 21(1):265–277

Publisher's Note Springer Nature remains neutral with regard to jurisdictional claims in published maps and institutional affiliations.

Feng-Yu Chu received his Ph.D. degree from the Department of Geomatics, National Cheng Kung University, Taiwan. His main research interests focus on multi-system multi-frequency GNSS precise positioning techniques, including navigation, RTK positioning, ambiguity resolution, precise point positioning, and long baseline computation. Moreover, he has completed a number of researches in geodesy, such as geodetic monitoring and datum determination. Currently, he is a postdoctoral researcher in the Department of Geomatics, National Cheng Kung University.

Ming Yang graduated with a B.Sc. degree in Surveying Engineering from National Cheng Kung University, Taiwan, and received his M.Sc. and Ph.D. degrees in Geodetic Science from The Ohio State University, USA. He has been working on GNSS-related researches since the 1990s. He is a professor in the Department of Geomatics, National Cheng Kung University and currently serves as the President of Geodetic Society of the Republic of China (Taiwan).

Yan-Ting Chen received his master's degree from the Department of Geomatics, National Cheng Kung University, Taiwan. His research interests include RTK positioning and navigation. In addition, he has completed research work on geodetic datum transformation and crustal deformation velocity field estimation. Currently, he is an associate technical specialist in Yunlin County Beigang Land Office, Taiwan.